Journal of Magnetism and Magnetic Materials 457 (2018) 75–82

Contents lists available at ScienceDirect

Journal of Magnetism and Magnetic Materials

journal homepage: www.elsevier.com/locate/jmmm

Research articles

Synthesis, characterization and microwave characteristics of ATP/$BaFe_{12}O_{19}$/PANI ternary composites

Dezhong Bai [a,1], Huixia Feng [a,b,*,1], Nali Chen [a,b], Lin Tan [a], Jianhui Qiu [c]

[a] College of Petrochemical Technology, Lanzhou University of Technology, Lanzhou 730050, China
[b] State Key Laboratory of Advanced Processing and Recycling of Nonferrous Metals, Lanzhou University of Technology, Lanzhou 730050, China
[c] Department of Machine Intelligence and Systems Engineering, Faculty of Systems Engineering, Akita Prefectural University, Akita 015-0055, Japan

ARTICLE INFO

Article history:
Received 27 July 2017
Received in revised form 18 December 2017
Accepted 31 December 2017
Available online 2 January 2018

Keywords:
Barium ferrite
Attapulgite
Polyaniline
Magnetism
Wave-absorbing property

ABSTRACT

In this paper, we introduced attapulgite (ATP) into the system of ferrite composites for the first time. By sol-gel self-propagating combustion method, attapulgite/barium ferrite (ATP/$BaFe_{12}O_{19}$) was prepared, and then ternary composites of attapulgite/barium ferrite/polyaniline (ATP/$BaFe_{12}O_{19}$/PANI) were obtained by in-situ oxidative polymerization of aniline on ATP/$BaFe_{12}O_{19}$ mixture. The phase composition, morphology and electromagnetic properties of the as-prepared composites were characterized by X-ray diffraction (XRD), Transmission election microscope (TEM), Fourier transform infrared (FTIR), vibrating sample magnetometer (VSM) and vector network analyzer (VNA). We found that the ATP/$BaFe_{12}O_{19}$/PANI composites at a thickness of 2 mm have the minimum reflection loss of −11.89 dB at 11.28 GHz, besides the effective absorption bandwidth (less than −5 dB) reached 6.39 GHz (from 8.42 GHz to 14.81 GHz).

1. Introduction

Electromagnetic (EM) interference has become a new source of pollution due to the extensive applications of modern electronic devices and communication facilities in the industrial, commercial, and military fields [1–3]. Therefore, the microwave absorption materials are the focus of extensive studies [4–7]. A suitable microwave absorbing materials own such advantages as tiny thickness, low density, good thermal stability and wide absorbing bandwidth.

Among ferrite magnets, hard magnetic barium ferrite ($BaFe_{12}O_{19}$) is widely used due to its high electrical resistivity, large magnetic crystalline anisotropy, high Curie temperature, low cost, excellent oxidation and corrosion resistance compared with other hard ferrites [8,9]. However, for $BaFe_{12}O_{19}$, due to its poor dielectric losses and fairly strong magnetic loss, which leads to poor matching of the dielectric loss and magnetic loss [10]. To overcome the shortcomings of the $BaFe_{12}O_{19}$, dielectric loss fillers such as conducting polymers, [11] carbon nanotubes [12,13], and graphene [14] are often added into the systems to obtain higher absorption intensity and broader frequency bandwidth.

Attapulgite (ATP) [$(Mg, Al)_4(Si)_8(O,OH,H_2O)_{26}{\cdot}nH_2O$] is a hydrated magnesium aluminum silicate presenting in nature as fibrillate mineral [15–17]. It may also be defined as crystalline material, wherein the atoms in layers are cross-linked by chemical bones, while the atoms of adjacent layers interact by physical forces [18–20]. As reported, ATP performs unusual absorption properties and shows potential applications as nanocomposites [21–23], catalyst supports [24–26], and sustainable absorbents [27]. The presence of micro-pores and channels in ATP structure and the nanorod-like morphology give a high surface area. Moreover, cation exchange capacity promotes commercial application of ATP [28].

As far as we know, the introduction of ATP into the ferrite absorber system has not yet been reported. Here in this report, the most inexpensive natural nanorods of ATP were surfaced-modified to be used as the structural strengthening agent. So the ternary ATP/$BaFe_{12}O_{19}$ composites were fabricated by sol-gel self-propagating combustion, and an additional process of in situ polymerization of aniline monomer was carried out for ATP/$BaFe_{12}O_{19}$/PANI composites. Furthermore, the contributions of impedance match and synergistic effects to enhance the microwave absorption properties were explored in detail.

* Corresponding author at: College of petrochemical Technology, Lanzhou University of Technology, Lanzhou 730050, China.
E-mail address: fenghx@lut.cn (H. Feng).
[1] These authors contributed equally to this work.

https://doi.org/10.1016/j.jmmm.2017.12.101
0304-8853/

2. Experimental

2.1. Materials

Attapulgite was obtained from Xuyi Botu Attapulgite Clay Co., Ltd. China (Mainland) Manufacturer, Trading Company. $Fe(NO_3)_3 \cdot 9H_2O$(≥98.5%), $Ba(NO_3)_2$(≥99.5%), citric acid (99.5%), ammonia aqueous solution, were purchased from Gansu Laiao Chemical Reagents Company, Gansu, China. Aniline (An) monomers were purified by distillation under reduced pressure before use. Other reagents were analytical grade and used without further purification. All solutions were prepared with distilled water.

2.2. The pretreatment and modification of ATP

The ATP mineral was first baked at 350 °C for 2 h in muffle furnace to remove organic compounds. It was then treated with 1 M HCl to activate its surface to get an activated ATP aqueous dispersion, the mixture was filtered and washed several times with distilled water until pH = 7. The sample was dried in a vacuum at 60 °C and then grounded.

2.3. Preparation of ATP/$BaFe_{12}O_{19}$ composites

The ATP/$BaFe_{12}O_{19}$ particles were prepared by sol-gel self-propagating combustion method [29]. Firstly, appropriate amount of $Fe(NO_3)_3 \cdot 9H_2O$, $Ba(NO_3)_2$ and citric acid were dissolved in 20 mL deionized water with vigorous stirring at room temperature. The molar ratio of solutes in the solution was Ba^{2+}:Fe^{3+}:$C_3H_4(OH)(COOH)_3$ = 1:12:15.6, pH value of the solution was adjusted to 7.0 with appropriate ammonia solution. 0.05 g ATP was added into the above prepared solution with ultrasonic 30 min and the mass fraction of ATP in the ATP/$BaFe_{12}O_{19}$ composite is 1.5 wt%. Next the mixture was evaporated at 80 °C in a water bath for 5 h to get bronzing sol, after that put the sol into air dry oven at 160 °C for 12 h to gain black dry gel. Then the dried gel burnt in air using self-propagating combustion manner until all gels are completely burnt out to form a loose powder. Grinding precursor powder was made by the above reaction. Finally the precursor powder was calcined at 1000 °C for 1 h in muffle furnace and cooled to room temperature to get the barium ferrite phase.

2.4. Preparation of ATP/$BaFe_{12}O_{19}$/PANI composites

ATP/$BaFe_{12}O_{19}$/PANI composites were prepared by in-situ chemical oxidation polymerization. The procedure was indicated as follows: firstly, 0.1 g ATP/$BaFe_{12}O_{19}$ composites was added in a 250 mL round-bottom flask contained 20 mL HCl (1M) solution and homogeneously dispersed under 30 min ultrasonic dispersion. Next, 1.0 g amido-sulfonic acid was dissolved in 20 mL distilled water to form amino sulfonic acid solution. 1 mL An monomer and amino sulfonic acid solution were added in round-bottom flask sequentially and equipped with a magnetic stirrer. After that 1.0 g ammonium peroxydisulfate (APS) was dissolved in 30 mL HCl solution, which was used as an oxidizing agent. The temperature of reaction system was controlled at 0–5 °C by using ice-bath. The APS solution was then slowly added drop-wise to initiate the polymerization. The polymerization was allowed to proceed for 6 h with magnetic stirring. ATP/$BaFe_{12}O_{19}$/PANI composites were obtained by filtering and washing the suspension with deionized water and absolute ethyl alcohol several times, dried under vacuum at 60 °C for 12 h. And the mass fraction of ATP/$BaFe_{12}O_{19}$ in ATP/$BaFe_{12}O_{19}$/PANI composites is 9%. The whole preparation process of ATP/$BaFe_{12}O_{19}$/PANI was illustrated in Scheme 1.

2.5. Characterization

The phase of sintered materials was confirmed by a powder X-ray diffraction technique (XRD, XRD-6000, Shimadzu Co., Ltd. Tokyo, Japan) equipped with Cu Kα as a radiation source (λ = 1.5406 Å). Each sample was scanned for 2θ range (5–90°) with a step size of 0.02°. The crystallite size was estimated from the width of the diffraction line, which corresponds to a particular reflection using the Scherrer equation. Fourier transform infrared spectroscopy (FTIR) analysis was performed at room temperature using a Nicolet 5700 spectrometer in transmission mode in the wavenumber range of 400–4000 cm^{-1}. The morphology of samples was observed using a transmission electron microscope (TEM, H-8110, Hitachi Co., Ltd. Tokyo, Japan). For this purpose, dispersions of nanoparticles were pipetted onto carbon-coated copper grids. A vibrating sample magnetometer (VSM, model Lake Shore, new 7304 series) was used to investigate the magnetic properties of the samples at room temperature. The maximum applied external field was 12 kOe.

2.6. EM absorption measurement

For EM absorption measurement, the samples were prepared by mixing the samples with paraffin wax at 70% weight fraction. The mixtures were then pressed into toroidal-shaped samples (Φ_{out} = 7.00 mm and Φ_{in} = 3.04 mm). The complex permittivity and permeability values were measured in the frequency range of 2.0–18 GHz range with the coaxial line method by an Agilent N5224A vector network analyzer.

3. Results and discussion

3.1. X-ray diffraction

Fig. 1 shows the XRD patterns of PANI, ATP, $BaFe_{12}O_{19}$, ATP/$BaFe_{12}O_{19}$, and ATP/$BaFe_{12}O_{19}$/PANI composite. It is known that the structure of PANI is predominately amorphous. The XRD pattern of PANI (Fig. 1a) appears at 2θ = 22.23°, which can be attributed to the periodicity and perpendicular to polymer chains of PANI [30]. The purified ATP displays diffraction peaks of 2θ = 8.36, 13.7, 16.4, 19.86, 20.8, 24.1, 26.66, 27.58 35.34, 42.06, 50.16, 54.8 and 61.4° (Fig. 1b), which are characteristic patterns of pure ATP and correspond to (1 1 0), (0 2 0), (3 1 0), (4 0 0), (2 1 1), (4 2 0), (3 2 1), (1 3 1), (0 5 0), (2 3 2), (0 7 0), (2 7 1) and (1 8 1) plane, respectively. All of these diffraction peaks are the same as those of the reference patterns collected for ATP (JCPDS 29-0855).

For barium ferrite (Fig. 1c), sharp diffraction peaks are observed at 2θ values of 30.62°, 32.48°, 34.40°, 37.40°, 40.64°, 42.68°, 55.30°, 56.82° 63.34°, 67.58°, and 72.80°, which correspond to the (1 1 0), (1 0 7), (1 1 4), (2 0 3), (2 0 5), (2 0 6), (2 1 7), (2011), (2 2 0), (2 0 1 4) and (3 1 7) reflections.[9,31,32] All the observed peaks of barium ferrite have been well matched with the standard XRD pattern (JCPDS No. 43-0002). This phenomenon demonstrates the phase barium ferrites are synthesized by sol-gel self-propagating combustion method. Average crystallite size (D) of the $BaFe_{12}O_{19}$ nanoparticles can be calculated from the highest intensity peak using Scherrer equation $D = k\lambda/\beta\cos\theta$, where k is Scherrer constant (k = 0.89), β is the full angular line width in radians at half maximum intensity, λ is wavelength of X-ray radiation, θ is the diffraction angle in degree [33]. The (1 1 4) reflection of the observed X-ray data was chosen for calculating the crystallite size of $BaFe_{12}O_{19}$ nanoparticles. The average size of the $BaFe_{12}O_{19}$ nanoparticles was calculated using the above mentioned equation and estimated at 41.8 nm.

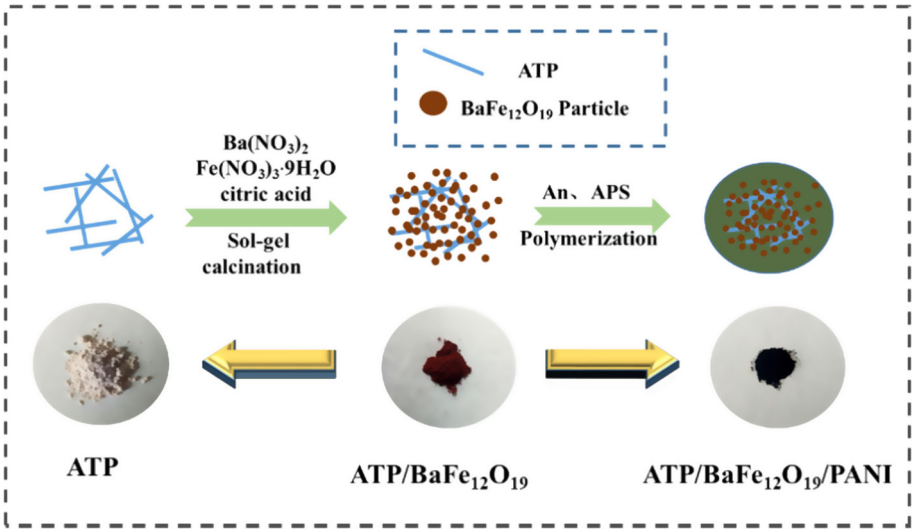

Scheme 1. Schematic illustration of the preparation process of ATP/$BaFe_{12}O_{19}$/PANI.

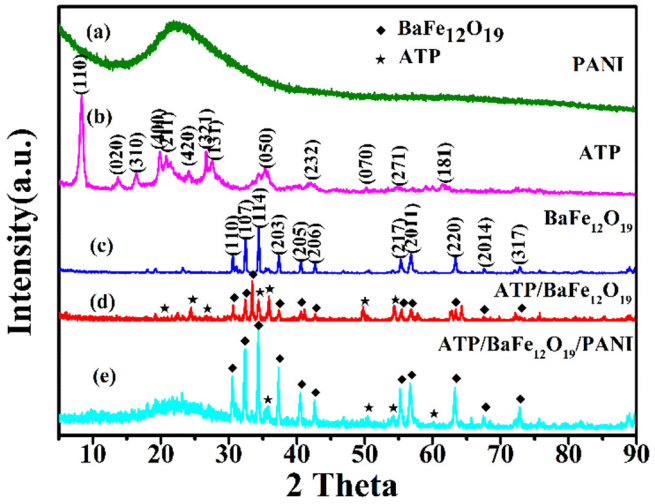

Fig. 1. XRD patterns of (a) PANI, (b) ATP, (c) $BaFe_{12}O_{19}$, (d) ATP/$BaFe_{12}O_{19}$, and (e) ATP/$BaFe_{12}O_{19}$/PANI.

As for the ATP/$BaFe_{12}O_{19}$ composite and ATP/$BaFe_{12}O_{19}$/PANI composite, the characteristic peaks of corresponding constituents can be easily found. These results indicate that the ATP/$BaFe_{12}O_{19}$ composite and the ATP/$BaFe_{12}O_{19}$/PANI composite have been successfully obtained.

3.2. FTIR spectra

As shown in Fig. 2, PANI, ATP, $BaFe_{12}O_{19}$, ATP/$BaFe_{12}O_{19}$, and ATP/$BaFe_{12}O_{19}$/PANI composites were characterized by FTIR spectroscopy (KBr pellet method) within the wave-length range 400–4000 cm^{-1}. For pure PANI (Fig. 2a), The spectrum of pure PANI reveals that the characteristic bands at 1650 cm^{-1} and 1490 cm^{-1} are attributed to the characteristic C=C stretching of the quinoid and benzenoid rings while the peaks at 1300 cm^{-1} is assigned to the C—N stretching of the secondary aromatic amine. The bands at 1130 cm^{-1} and 796 cm^{-1} can be ascribed to out-of-plane bending of C—H [34–36]. The broad peak around 3460 cm^{-1} is attributable to the N—H stretching mode[37].

For acid activated ATP (Fig. 2b), the structural OH stretching vibrations appear in the range of 3700–3200 cm^{-1}, which confirms

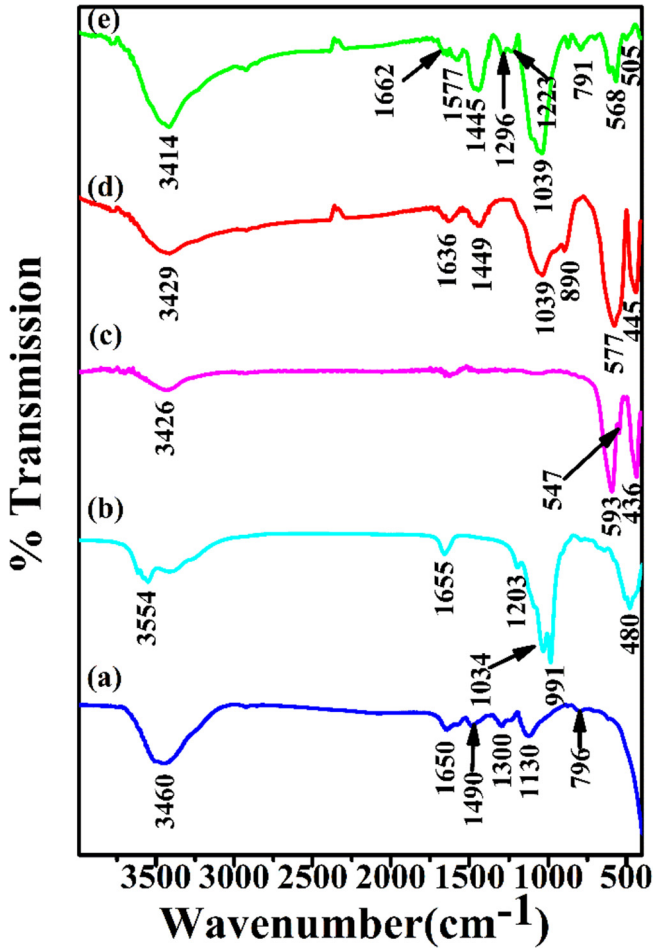

Fig. 2. FT-IR spectra of (a) PANI, (b) ATP, (c) $BaFe_{12}O_{19}$, (d) ATP/$BaFe_{12}O_{19}$, and (e) ATP/$BaFe_{12}O_{19}$/PANI.

a great amount of active hydroxyl groups existing on the surface of ATP. The band located at 3620 cm^{-1} is attributed to the stretching vibration of OH associated with Al^{3+} cations in dioctahedral coordination (Al_2OH) and to the OH stretching vibration of water coordinated to Mg along the fibers. The peak at 3554 cm^{-1} is related to

the stretching vibrations of OH in (Al, Mg)–OH [26,38]. The peak at 1655 cm^{-1} is attributed to bending vibration of water molecules which acts as adsorbed ligands. Three characteristic peaks at 1203, 1034 and 991 cm^{-1} are caused by stretching vibration of the Si—O—Si bonds, and the peak at 480 cm^{-1} is attributed to the bending vibration of Si—O—Si bonds.[39]

The FTIR spectrum of $BaFe_{12}O_{19}$ (Fig. 2c) shows characteristic peaks at 436 cm^{-1}, 547 cm^{-1}, 593 cm^{-1}, which are attributed to the Fe—O bond stretching vibration.[31] After mixing with ATP (Fig. 2d), we can see that the characteristic absorption peak of $BaFe_{12}O_{19}$ and ATP all exist at ATP/$BaFe_{12}O_{19}$ composites. Compared with the FT-IR spectrum of PANI (Fig. 3a), the peaks at 1650, 1490, 1300 and 796 cm^{-1} are red shifted to 1577, 1445, 1296 and 791 cm^{-1} in the ATP/$BaFe_{12}O_{19}$/PANI composite, suggesting the successful coating of PANI on the surfaces of ATP/$BaFe_{12}O_{19}$. The red shift of the vibrations may have three points: (1) the π molecular orbital of PANI overlaps the empty d-orbital of Fe^{3+} in barium ferrite to form the σ-bond where metal ions play a role of the electron pair acceptor; (2) the π^* molecular orbital of PANI overlaps the empty d-orbital of Fe^{3+} to form the π-bond, in which the Fe^{3+} is the electron pair donor; and (3) the presence of solid state charge transfer in ATP and PANI, ATP as the cation acceptor, the surface of sheets has electronegativity, but the existence of emeraldine salt form of PANI as cation having electropositivity. Therefore, the electron transfer balance between the PANI molecular chain and surface of $BaFe_{12}O_{19}$ easily forms electron transfer complex [32,40]. Meanwhile, the characteristic peaks of ATP (Fig. 3b) at 1655, 1203, 1034 and 480 cm^{-1} blue shifted to 1662, 1223, 1039 and 505 cm^{-1} in the ATP/$BaFe_{12}O_{19}$/PANI composite, indicating that there exists a charge transfer between PANI and ATP.[41]

FTIR results indicate that the characteristic bands of $BaFe_{12}O_{19}$, ATP and PANI are present in the ternary composite spectrum, and the intermolecular interactions exist between these three components.

3.3. Morphology

The TEM images of $BaFe_{12}O_{19}$, ATP/$BaFe_{12}O_{19}$ and ATP/$BaFe_{12}O_{19}$/PANI composites are presented in Fig. 3. Fig. 3a shows the micromorphology of $BaFe_{12}O_{19}$ nanoparticles; it can be clearly seen that $BaFe_{12}O_{19}$ nanoparticles are highly agglomerated with particle size in the range of 20–80 nm due to the magnetic dipole interaction between ferrite particles [42]. The image exhibits that the nanoparticles of $BaFe_{12}O_{19}$ are hexagonal approximately. At the same time, we can see that the particles size of materials are not uniform and its distribution is extremely different.

From Fig. 3b and c, we can see that there are a large number of ferrite particles with a size of several tens of nanometers accumulated on the surface of ATP. TEM images of ATP/$BaFe_{12}O_{19}$/PANI (Fig. 3d) indicate that the in-situ chemical oxidation polymerization process leads to the formation of core-shell type morphology with ATP/$BaFe_{12}O_{19}$ as the center while the polymer (PANI) forms the covering. The shell of the particles gives an impression of an amorphous layer, as no fringes have been observed at the shell.

3.4. Magnetic properties

The magnetic properties of the $BaFe_{12}O_{19}$, ATP/$BaFe_{12}O_{19}$ and ATP/$BaFe_{12}O_{19}$/PANI composites were determined by VSM analysis at room temperature, and their magnetic hysteresis loops are shown in Fig. 4. The magnetic parameters such as saturation magnetization (Ms), remnant magnetization (Mr) and coercivity (Hc) of samples determined by the hysteresis loops obtained from Fig. 4 are listed in Table 1. It is striking to note that $BaFe_{12}O_{19}$ particles and all the composites behave as a broad hysteresis loop at room temperature, indicating the ferromagnetic behavior of them. What is more, it can be seen that the Ms, Mr. and Hc value of pure $BaFe_{12}O_{19}$ ferrite reached 54.973 emu/g, 5.45 kOe, 32.128 emu/g, respectively. Due to the fact that ATP and PANI are non-magnetic the Ms, Mr. and Hc value of ATP/$BaFe_{12}O_{19}$ composite and ATP/$BaFe_{12}O_{19}$/

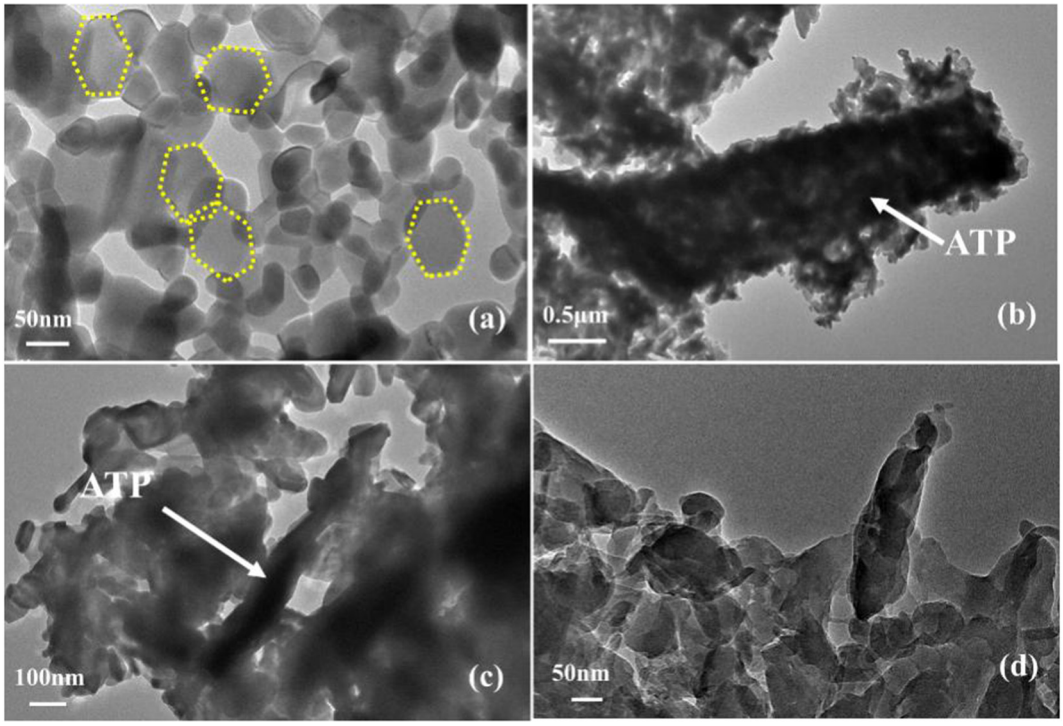

Fig. 3. TEM images of (a) $BaFe_{12}O_{19}$, (b and c) ATP/$BaFe_{12}O_{19}$, and (d) ATP/$BaFe_{12}O_{19}$/PANI.

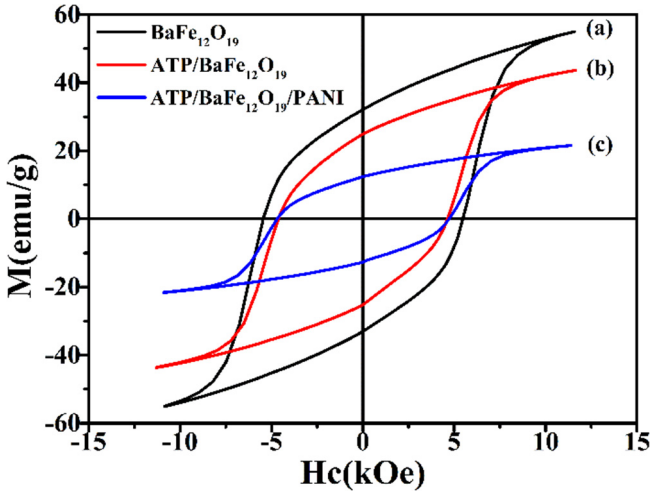

Fig. 4. Magnetic hysteresis loops of (a) $BaFe_{12}O_{19}$, (b) ATP/$BaFe_{12}O_{19}$, and (c) ATP/$BaFe_{12}O_{19}$/PANI.

Table 1
Saturation magnetization (Ms), remnant magnetization (Mr) and coercivity (Hc) of samples.

Samples	Hc(kOe)	Mr(emu/g)	Ms(emu/g)
(a) $BaFe_{12}O_{19}$	5.450	32.128	54.973
(b) ATP/$BaFe_{12}O_{19}$	4.616	24.968	43.643
(c) ATP/$BaFe_{12}O_{19}$/PANI	4.685	12.434	21.573

PANI composite are lower than those of pure $BaFe_{12}O_{19}$ powder. Generally, the coercivity of a material depends upon many factors, such as grain shape, morphology, structure, composition, magnetocrystalline anisotropy and magnetostriction [43].

As a natural clay material, ATP is an ideal support because of its high-specific surface area as well as abundant active sites [20,44]. For the ATP/$BaFe_{12}O_{19}$/PANI composites, firstly, in the polymerization process, the $BaFe_{12}O_{19}$ particles adhere to the surface of ATP. After that PANI is deposited on the ATP/$BaFe_{12}O_{19}$ surface and crystallite boundaries, which would result in an interface effect between the PANI and ATP/$BaFe_{12}O_{19}$, therefore the surface anisotropy of the ATP/$BaFe_{12}O_{19}$/PANI composites declines [45]. Secondly, in M-type barium ferrites, lowering the anisotropy field results in lower natural resonance frequency [46–48]. The PANI coating on the ATP/$BaFe_{12}O_{19}$ nanoparticles will likely affect the contributions of the surface anisotropy, shape anisotropy, and interface anisotropy to the net anisotropy [49]. Consequently, the ATP/$BaFe_{12}O_{19}$/PANI composites show lower coercivity value compared to that of pure barium ferrite.

3.5. Microwave absorbing properties

The non-magnetic paraffin wax has been used to prepare the ring due to its ultralow dielectric parameters [50]. Through the analysis of previous related literatures [10,13,51], we carried out a preliminary test on the mixing ratio of the sample and paraffin wax. When the amount of paraffin wax is too high, the percentage of sample particles will be reduced, which will lead to the decrease of absorbing property. When the amount of paraffin is too low, the mixture is excessively viscous and dried so that it is difficult to press into the ring, and a large number of holes are formed after molding. Therefore, the test samples for the complex permeability and permittivity were prepared by mixing the sample (70 wt%) with paraffin matrix, and then pressing the mixture into a cylindrical shaped compact(Φ_{out} = 7.00 mm and Φ_{in} = 3.04 mm). The EM properties of the $BaFe_{12}O_{19}$, ATP/$BaFe_{12}O_{19}$ and ATP/$BaFe_{12}O_{19}$/PANI composites were investigated in the frequency range from 2 to 18 GHz in this study.

As is well known, the real parts (ε', μ') of complex permittivity and permeability represent the storage of the electric and magnetic energy, respectively. While the imaginary parts (ε'', μ'') of complex permittivity and permeability symbolize the loss of the electric and magnetic energy. As a microwave absorber, big imaginary parts of complex permittivity and permeability are expected [52].

The real (μ') and the imaginary (μ'') parts of the relative complex permeability are shown in panels a and b in Fig. 5, respectively, together with the tangent magnetic loss angle (tan δ_M, tan $\delta_M = \mu''/\mu'$) of the composites in Fig. 5c. It is noted in Fig. 5a–c that the as-synthesized $BaFe_{12}O_{19}$, ATP/$BaFe_{12}O_{19}$ and ATP/$BaFe_{12}O_{19}$/PANI composites show the similar frequency-dependent permeability. As shown in Fig. 5a, it can be seen that the complex permeability real part (μ') of the $BaFe_{12}O_{19}$, ATP/$BaFe_{12}O_{19}$ and ATP/$BaFe_{12}O_{19}$/PANI composites have four evident fluctuations at about ~3.4, 6.6, 13.6 and 15.5 GHz. For the variations in μ'' as a function of frequency shown in Fig. 5b, three curves of μ'' intersect at ~10 GHz. Before the intersection, all of the three curves behave as obvious decline in the frequency range from 2 to 10 GHz, the μ'' of $BaFe_{12}O_{19}$ higher than ATP/$BaFe_{12}O_{19}$ and ATP/$BaFe_{12}O_{19}$/PANI composites. However, after the intersection, we can see that all of the three curves behave as obvious elevation in the frequency range from 10 to 18 GHz, the μ'' of $BaFe_{12}O_{19}$ lower than ATP/$BaFe_{12}O_{19}$ and ATP/$BaFe_{12}O_{19}$/PANI composites. The energy loss caused by magnetic relaxation can be more clearly evaluated by tan δ_M, which is also plotted as a function of frequency as shown in Fig. 5c. The shapes and the tendencies of the tan δ_M vs frequency are almost the same with those of the μ'' vs frequency.

The variation in ε', ε'', and the tangent of dielectric loss angle (tan δ_E, tan $\delta_E = \varepsilon''/\varepsilon'$) as a function of frequency of the samples are shown in Fig. 5d–f, respectively. Fig. 5d and e show the ε' and ε'' for $BaFe_{12}O_{19}$ particles and ATP/$BaFe_{12}O_{19}$, ATP/$BaFe_{12}O_{19}$/PANI composites. It is noted that the ε' for raw $BaFe_{12}O_{19}$ is nearly about 4.3 and the ε'' is nearly about 0.5, indicating that the dielectric losses of $BaFe_{12}O_{19}$ are very poor [53]. After mixing with ATP and PANI, the value of the complex dielectric permittivity of the ATP/$BaFe_{12}O_{19}$, ATP/$BaFe_{12}O_{19}$/PANI composites become higher than the $BaFe_{12}O_{19}$. The dielectric performance of the material depends on ionic, electronic, orientational (arising due to the presence of bound charges) and space charge polarization (due to the heterogeneity in the system). In a heterogeneous system, the accumulation of virtual charges at the interface of two media having different dielectric constants, ε_1' and ε_2', and conductivities σ_1 and σ_2, respectively, leads to interfacial polarization and is known as Maxwell–Wagner polarization [40]. Here, ATP along with the $BaFe_{12}O_{19}$ nanoparticles were incorporated in the polyaniline matrix and therefore show interfacial polarization in the applied frequency range. The presence of insulating $BaFe_{12}O_{19}$ in the conducting matrix results in the formation of an increased interface at a heterogeneous system, wherein some space charge accumulates at the interface, contributing to the higher microwave absorption. For the ATP/$BaFe_{12}O_{19}$/PANI composites, the observed decrease in ε' with increasing frequency may be attributed to the decrease in space charge polarization with increasing frequency [54]. In addition, it can be seen in the frequency dependence of tan δ_E for the ATP/$BaFe_{12}O_{19}$ and ATP/$BaFe_{12}O_{19}$/PANI composites in Fig. 5f, where the tan δ_E of the ATP/$BaFe_{12}O_{19}$ and ATP/$BaFe_{12}O_{19}$/PANI composites higher than the pure $BaFe_{12}O_{19}$ in the range from 2 to 18 GHz. The observed tan δ_E For ATP/$BaFe_{12}O_{19}$/PANI composites reaches up to ~0.24 at 2 GHz and stays higher than tan δ_M = ~0.22 (Fig. 5c and f), still higher than the magnetic loss, which indicates that dielectric loss makes major contribution to the electromagnetic loss.

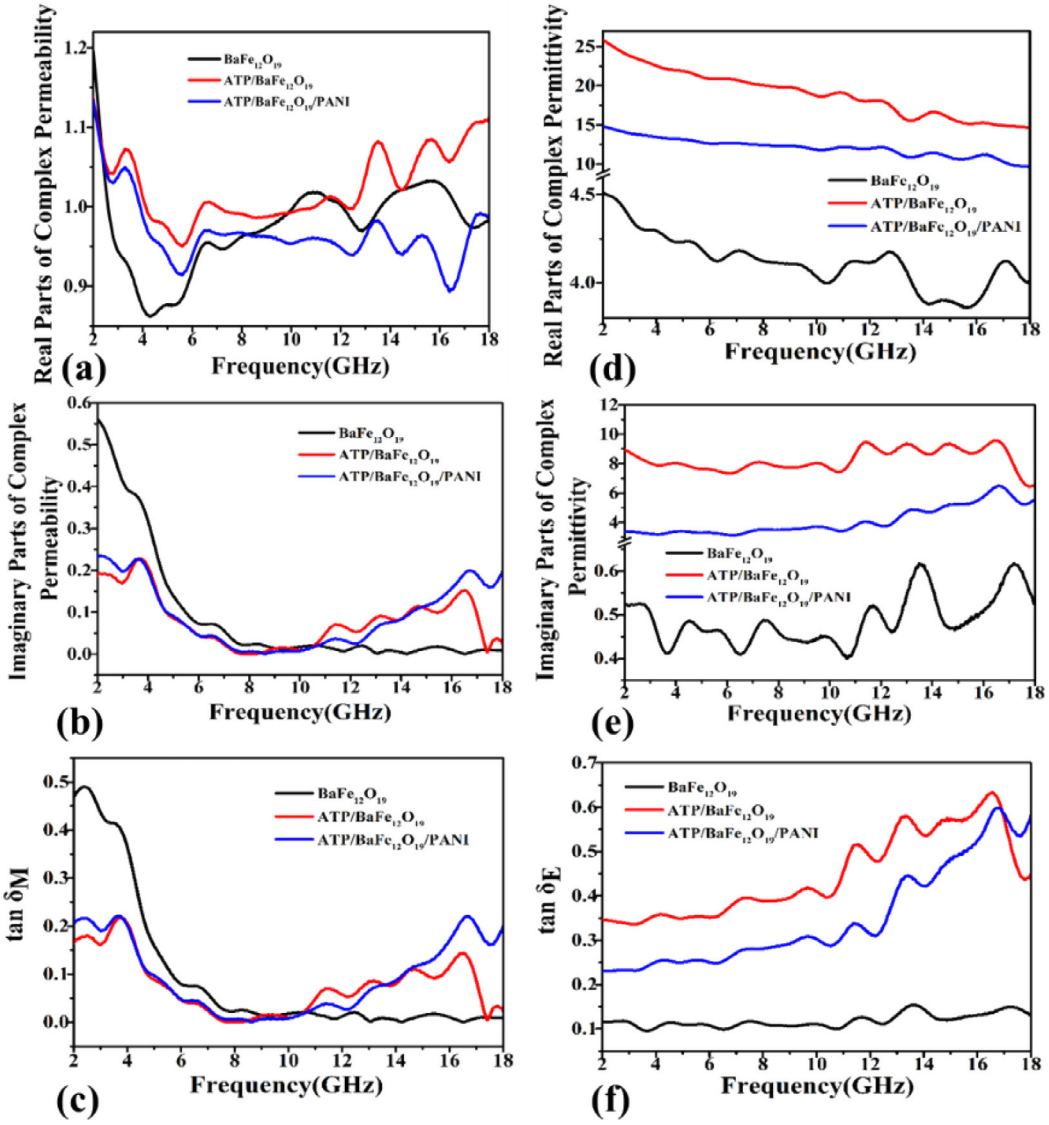

Fig. 5. Measured relative (a and b) complex permeability, (d and e) complex permittivity and (c and f) magnetic and dielectric loss values of $BaFe_{12}O_{19}$, ATP/$BaFe_{12}O_{19}$, ATP/$BaFe_{12}O_{19}$/PANI.

As the EM adsorption performance depends on not only the loss of magnetic and dielectric but also the proper matching of the dielectric and the magnetic properties, the final EM efficiency of the as-synthesized composites were evaluated by the reflection loss of the samples based on transmission line theory [55]. According to this theory, when the EM wave transmits through a medium, there are many factors affected the reflectivity, such as μ, ε, sample thickness, and EM wave frequency. The reflection loss (RL) can be calculated from the equations shown below.

$$Zin = Z0\sqrt{\frac{\mu}{\varepsilon}}\tanh\left[j\left(\frac{2\pi fd}{c}\right)\sqrt{\mu\varepsilon}\right] \quad (1)$$

$$RL = 20\lg\left|\frac{Z_{in}-Z_0}{Z_{in}+Z_0}\right| \quad (2)$$

where f is the microwave frequency, d is the thickness of the absorber, c is the velocity of light, Z_{in} is represent for the input of the absorber and Z_0 is the impedance in free space. It can be seen that the electromagnetic wave absorption capacity of materials are closely related to electromagnetic parameters of materials (ε′, ε″, μ′, μ″, d and f). The reflection loss of the same material is mainly determined by the thickness of the material at the same frequency. Therefore, in order to design an EM wave absorber, the control of the frequency dependencies of the relative complex permeability μ and the relative complex permittivity ε is of significance.

In order to study the microwave absorption performance in-depth, Fig. (6a, b and c) shows the reflection losses of pure $BaFe_{12}O_{19}$, ATP/$BaFe_{12}O_{19}$, and ATP/$BaFe_{12}O_{19}$/PANI composites with different matching thicknesses at 2–18 GHz; It can be found that the microwave properties of samples under the matching thickness of 1–5 mm. With increasing the thickness of absorbent layer, from Fig. 6a, b and c, one can see that the minimum RL value of pure $BaFe_{12}O_{19}$, ATP/$BaFe_{12}O_{19}$ and ATP/$BaFe_{12}O_{19}$/PANI composites increases at first and then decreases. The optimal RL values of pure $BaFe_{12}O_{19}$, ATP/$BaFe_{12}O_{19}$, and ATP/$BaFe_{12}O_{19}$/PANI composites are −10.7 dB at 13.56 GHz with an absorbent layer thickness of 3 mm, −6.8 dB at 8.92 GHz with an absorbent layer thickness of 2 mm and −12.37 dB at 6.98 GHz with an absorbent layer thickness of 3 mm, respectively. The ATP/$BaFe_{12}O_{19}$ (Fig. 6b) shows a little

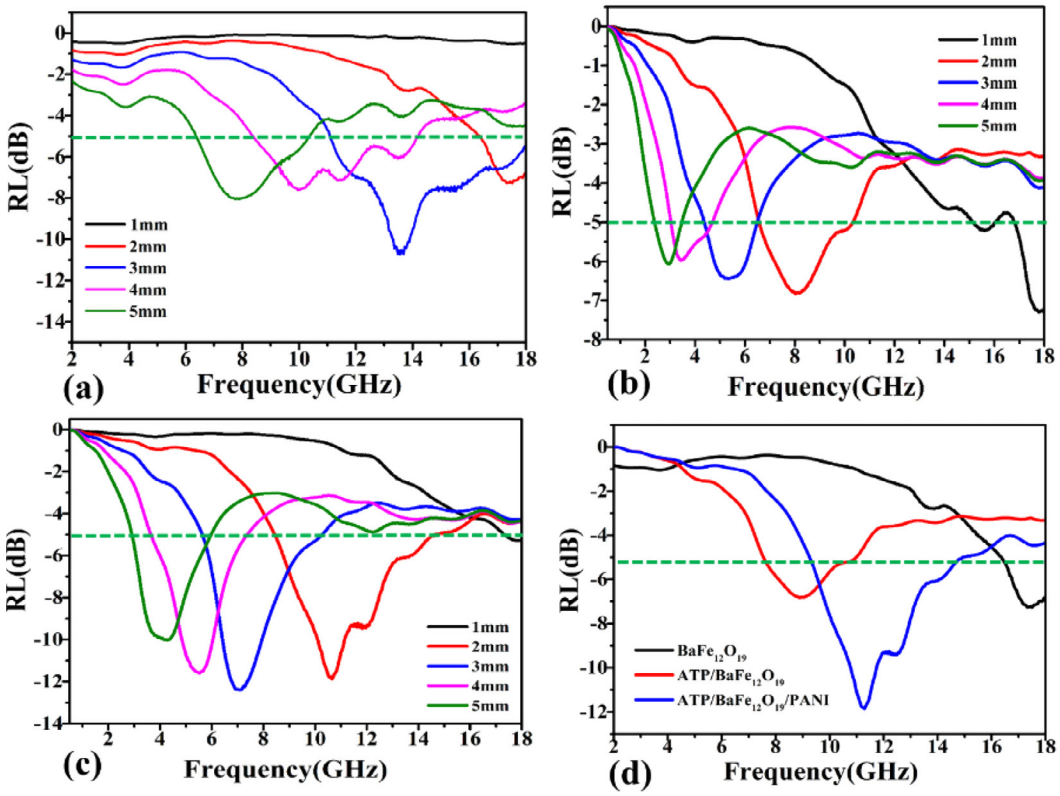

Fig. 6. Microwave RL curves of (a) $BaFe_{12}O_{19}$, (b) ATP/$BaFe_{12}O_{19}$, (c) ATP/$BaFe_{12}O_{19}$/PANI with different thicknesses at 2–18 GHz; (d) Microwave RL curves of $BaFe_{12}O_{19}$, ATP/$BaFe_{12}O_{19}$, and ATP/$BaFe_{12}O_{19}$/PANI of 2 mm at 2–18 GHz.

worse behavior for electromagnetic loss at 2–18 GHz frequency. Besides, the minimum RL of samples shifts toward lower frequency with increasing sample thickness.

And Fig. 6d shows microwave RL curves of $BaFe_{12}O_{19}$, ATP/$BaFe_{12}O_{19}$, ATP/$BaFe_{12}O_{19}$/PANI composites with a thickness of 2 mm at 2–18 GHz. The absorbing properties minimum RL of pure $BaFe_{12}O_{19}$ nanoparticles is −7.28 dB at 17.32 GHz, and bandwidth under −5 dB is approximately 1.64 GHz. It is noted that the absorbing properties of ATP/$BaFe_{12}O_{19}$/PANI composite are improved when ATP/$BaFe_{12}O_{19}$ was packed by PANI, the minimum RL value is −11.89 dB at 11.28 GHz and the effective absorption bandwidth (less than −5 dB) reached 6.39 GHz (from 8.42 GHz to 14.81 GHz). Compared with our previous work [29], the absorbing performance of this composite is obviously improved (the absorption peak increased from −5.66 dB to −11.89 dB). This may be due to synergistic effects of ATP, $BaFe_{12}O_{19}$, and PANI play an important role for enhancing the absorbing properties of ATP/$BaFe_{12}O_{19}$/PANI composites.

4. Conclusions

In summary, barium ferrite nanoparticles were distributed and anchored onto the surface of the ATP, which have prepared ATP/$BaFe_{12}O_{19}$ composite by sol-gel self-propagating combustion method. And the ternary composite based on ATP/$BaFe_{12}O_{19}$/PANI have been prepared and investigated. The introduced ATP and PANI generated resonance in complex permittivity and permeability as well as sufficiently enhanced dielectric loss, resulting in enhancing microwave absorption performance and widening effective absorption bandwidth. We found that the ATP/$BaFe_{12}O_{19}$/PANI composites at a thickness of 2 mm have the minimum reflection loss of −11.89 dB at 11.28 GHz, and the effective absorption bandwidth (less than −5 dB) reached 6.39 GHz (from 8.42 GHz to 14.81 GHz). This represents a new idea for further studies of ATP for application as microwave-absorbing materials.

Acknowledgments

We are grateful for financial support from the National Natural Science Foundation of China (NSFC. 21664009, 51063003), the Ministry of Science and Technology project (No. 2009GJG10041), the Fundamental Research Funds for the Universities of Gansu (No. 1105ZTC136), the Natural Science Foundation of Gansu Province (No. 1208RJZA173).

References

[1] L. Kong, X. Yin, Y. Zhang, X. Yuan, Q. Li, F. Ye, L. Cheng, L. Zhang, Electromagnetic wave absorption properties of reduced graphene oxide modified by maghemite colloidal nanoparticle clusters, J. Phys. Chem. C 117 (2013) 19701–19711.
[2] X. Sun, J. He, G. Li, J. Tang, T. Wang, Y. Guo, H. Xue, Laminated magnetic graphene with enhanced electromagnetic wave absorption properties, J. Mater. Chem. C 1 (2013) 765–777.
[3] F. Ren, H. Yu, L. Wang, M. Saleem, Z. Tian, P. Ren, Current progress on the modification of carbon nanotubes and their application in electromagnetic wave absorption, RSC Adv. 4 (2014) 14419.
[4] Y. Zhang, Y. Huang, T. Zhang, H. Chang, P. Xiao, H. Chen, Z. Huang, Y. Chen, Broadband and tunable high-performance microwave absorption of an ultralight and highly compressible graphene foam, Adv. Mater. 27 (2015) 2049–2053.
[5] M.S. Cao, J. Yang, W.L. Song, D.Q. Zhang, B. Wen, H.B. Jin, Z.L. Hou, J. Yuan, Ferroferric oxide/multiwalled carbon nanotube vs polyaniline/ferroferric oxide/multiwalled carbon nanotube multiheterostructures for highly effective microwave absorption, ACS Appl. Mater. Interfaces 4 (2012) 6949–6956.
[6] M. Han, X. Yin, L. Kong, M. Li, W. Duan, L. Zhang, L. Cheng, Graphene-wrapped ZnO hollow spheres with enhanced electromagnetic wave absorption properties, J. Mater. Chem. A 2 (2014) 16403–16409.

[7] M. Fu, Q. Jiao, Y. Zhao, Preparation of $NiFe_2O_4$ nanorod-graphene composites via an ionic liquid assisted one-step hydrothermal approach and their microwave absorbing properties, J. Mater. Chem. A 1 (2013) 5577.

[8] M. Drofenik, I. Ban, D. Makovec, A. Žnidaršič, Z. Jagličić, D. Hanžel, D. Lisjak, The hydrothermal synthesis of super-paramagnetic barium hexaferrite particles, Mater. Chem. Phys. 127 (2011) 415–419.

[9] M. Verma, A.P. Singh, P. Sambyal, B.P. Singh, S.K. Dhawan, V. Choudhary, Barium ferrite decorated reduced graphene oxide nanocomposite for effective electromagnetic interference shielding, PCCP 17 (2015) 1610–1618.

[10] T. Zhao, X. Ji, W. Jin, C. Wang, W. Ma, J. Gao, A. Dang, T. Li, S. Shang, Z. Zhou, Direct in situ synthesis of a 3D interlinked amorphous carbon nanotube/graphene/$BaFe_{12}O_{19}$ composite and its electromagnetic wave absorbing properties, RSC Adv. 7 (2017) 15903–15910.

[11] T. Ben Ghzaiel, W. Dhaoui, A. Pasko, F. Mazaleyrat, Optimization of multiroute synthesis for polyaniline-barium ferrite composites, Mater. Chem. Phys. 179 (2016) 42–54.

[12] T. Zhao, W. Jin, X. Ji, H. Yan, Y. Jiang, Y. Dong, Y. Yang, A. Dang, H. Li, T. Li, S. Shang, Z. Zhou, Synthesis of sandwich microstructured expanded graphite/barium ferrite connected with carbon nanotube composite and its electromagnetic wave absorbing properties, J. Alloy. Compd. 712 (2017) 59–68.

[13] T. Zhao, X. Ji, W. Jin, S. Guo, H. Zhao, W. Yang, X. Wang, C. Xiong, A. Dang, H. Li, T. Li, S. Shang, Z. Zhou, Electromagnetic wave absorbing properties of aligned amorphous carbon nanotube/$BaFe_{12}O_{19}$ nanorod composite, J. Alloy. Compd. 703 (2017) 424–430.

[14] T. Zhao, X. Ji, W. Jin, C. Xiong, W. Ma, C. Wang, S. Duan, A. Dang, H. Li, T. Li, S. Shang, Z. Zhou, Synthesis and electromagnetic wave absorption property of amorphous carbon nanotube networks on a 3D graphene aerogel/$BaFe_{12}O_{19}$ nanocomposite, J. Alloy. Compd. 708 (2017) 115–122.

[15] J.H. Xu, D.X. Tan, L.Y. Yan, Z. Li, Preparation and swelling properties of P(AMPS-co-AM)/attapulgite clay superabsorbent composite by microwave irradiation, Adv. Mater. Res. 512–515 (2012) 2394–2398.

[16] G.N. Pshinko, T.G. Timoshenko, A.A. Bogolepov, Effect of fulvic acids on Th(IV) sorption on montmorillonite, Radiochemistry 51 (2009) 91–95.

[17] L. Tan, X. Wang, X. Tan, H. Mei, C. Chen, T. Hayat, A. Alsaedi, T. Wen, S. Lu, X. Wang, Bonding properties of humic acid with attapulgite and its influence on U(VI) sorption, Chem. Geol. (2017).

[18] R.A. Schoonheydt, T. Pinnavaia, G. Lagaly, N. Gangas, Pillared clays and pillared layered solids, Pure Appl. Chem. Commun. 71 (1999) 2367–2371.

[19] B. Chen, J.R. Evans, H.C. Greenwell, P. Boulet, P.V. Coveney, A.A. Bowden, A. Whiting, A critical appraisal of polymer-clay nanocomposites, Chem. Soc. Rev. 37 (2008) 568–594.

[20] C.H. Zhou, An overview on strategies towards clay-based designer catalysts for green and sustainable catalysis, Appl. Clay Sci. 53 (2011) 87–96.

[21] L.F. Chen, H.W. Liang, Y. Lu, C.H. Cui, S.H. Yu, Synthesis of an attapulgite clay@carbon nanocomposite adsorbent by a hydrothermal carbonization process and their application in the removal of toxic metal ions from water, Langmuir 27 (2011) 8998–9004.

[22] X. Liu, R. Wang, Effective removal of hydrogen sulfide using 4A molecular sieve zeolite synthesized from attapulgite, J. Hazard. Mater. 326 (2017) 157–164.

[23] P. Liu, L. Jiang, L. Zhu, A. Wang, Attapulgite/poly(acrylic acid) nanocomposite (ATP/PAA) hydrogels with multifunctionalized attapulgite (org-ATP) nanorods as unique cross-linker: preparation optimization and selective adsorption of Pb(II) ion, ACS Sustain. Chem. Eng. 2 (2014) 643–651.

[24] J.-L. Cao, G.-S. Shao, Y. Wang, Y. Liu, Z.-Y. Yuan, CuO catalysts supported on attapulgite clay for low-temperature CO oxidation, Catal. Commun. 9 (2008) 2555–2559.

[25] L. Li, F. Chen, J. Shao, Y. Dai, J. Ding, Z. Tang, Attapulgite clay supported Ni nanoparticles encapsulated by porous silica: thermally stable catalysts for ammonia decomposition to CO_x free hydrogen, Int. J. Hydrogen Energy 41 (2016) 21157–21165.

[26] L. Lu, X.-Y. Li, X.-Q. Liu, Z.-M. Wang, L.-B. Sun, Enhancing the hydrostability and catalytic performance of metal-organic frameworks by hybridizing with attapulgite, a natural clay, J. Mater. Chem. A 3 (2015) 6998–7005.

[27] Y. Kong, J. Yuan, Z. Wang, S. Yao, Z. Chen, Application of expanded graphite/attapulgite composite materials as electrode for treatment of textile wastewater, Appl. Clay Sci. 46 (2009) 358–362.

[28] W. Wu, C. Cai, Y. Li, Y. Chen, Y. Gao, Y. Zhao, W. Ren, Impact of attapulgite clay on the phases and structures of novel woodceramics, RSC Adv. 6 (2016) 103042–103048.

[29] H.X. Feng, D.Z. Bai, L. Tan, N.L. Chen, Y.Y. Wang, Preparation and microwave-absorbing property of EP/$BaFe_{12}O_{19}$/PANI composites, J. Magn. Magn. Mater. 433 (2017) 1–7.

[30] X. Meng, Y. Zhu, S. Xu, T. Liu, Facile synthesis of shell-core polyaniline/$SrFe_{12}O_{19}$ composites and magnetic properties, RSC Adv. 6 (2016) 4946–4949.

[31] A. Ohlan, K. Singh, A. Chandra, S.K. Dhawan, Microwave absorption behavior of core-shell structured poly (3,4-ethylenedioxy thiophene)-barium ferrite nanocomposites, ACS Appl. Mater. Interfaces 2 (2010) 927–933.

[32] J. Luo, P. Shen, W. Yao, C. Jiang, J. Xu, Synthesis, Characterization, and microwave absorption properties of reduced graphene oxide/strontium ferrite/polyaniline nanocomposites, Nanoscale Res. Lett. 11 (2016) 141.

[33] P. Sambyal, A.P. Singh, M. Verma, M. Farukh, B.P. Singh, S.K. Dhawan, Tailored polyaniline/barium strontium titanate/expanded graphite multiphase composite for efficient radar absorption, RSC Adv. 4 (2014) 12614.

[34] H. Yang, N. Han, Y. Lin, G. Zhang, L. Wang, Enhanced microwave absorbing properties of PANI/$CoFe_2O_4$/PVDF composite, RSC Adv. 6 (2016) 100585–100589.

[35] Y.G. Wang, H.Q. Li, Y.Y. Xia, Ordered whiskerlike polyaniline grown on the surface of mesoporous carbon and its electrochemical capacitance performance, Adv. Mater. 18 (2006) 2619–2623.

[36] J.T. Zhang, X.S. Zhao, Conducting polymers directly coated on reduced graphene oxide sheets as high-performance supercapacitor electrodes, J. Phys. Chem. C 116 (2012) 5420–5426.

[37] G. Ma, Y. Chen, L. Li, D. Jiang, R. Qiao, Y. Zhu, An attractive photocatalytic inorganic antibacterial agent: Preparation and property of graphene/zinc ferrite/polyaniline composites, Mater. Lett. 131 (2014) 38–41.

[38] L. Boudriche, R. Calvet, B. Hamdi, H. Balard, Effect of acid treatment on surface properties evolution of attapulgite clay: an application of inverse gas chromatography, Colloids Surf. A 392 (2011) 45–54.

[39] P. Wu, D. Deng, H. Zhang, C. Cai, Electrochemical detection of trinitrotoluene in water samples based on a natural mineral attapulgite modified electrode, J. Electroanal. Chem. 781 (2016) 238–244.

[40] K. Singh, A. Ohlan, V.H. Pham, B.R.S. Varshney, J. Jang, S.H. Hur, W.M. Choi, M. Kumar, S.K. Dhawan, B.S. Kong, J.S. Chung, Nanostructured graphene/Fe_3O_4 incorporated polyaniline as a high performance shield against electromagnetic pollution, Nanoscale 5 (2013) 2411–2420.

[41] Z.-F. Li, H. Zhang, Q. Liu, Y. Liu, L. Stanciu, J. Xie, Covalently-grafted polyaniline on graphene oxide sheets for high performance electrochemical supercapacitors, Carbon 71 (2014) 257–267.

[42] X. Tang, Y. Yang, Surface modification of M-Ba-ferrite powders by polyaniline: towards improving microwave electromagnetic response, Appl. Surf. Sci. 255 (2009) 9381–9385.

[43] Q. Song, Z.J. Zhang, Shape control and associated magnetic properties of spinel cobalt ferrite nanocrystals, J. Am. Chem. Soc. 126 (2004) 6164–6168.

[44] X. Li, X. Yan, S. Zuo, X. Lu, S. Luo, Z. Li, C. Yao, C. Ni, Construction of $LaFe_{1-x}Mn_xO_3$/attapulgite nanocomposite for photo-SCR of NO_x at low temperature, Chem. Eng. J. 320 (2017) 211–221.

[45] K. Chen, C. Xiang, L. Li, H. Qian, Q. Xiao, F. Xu, A novel ternary composite fabrication, performance and application of expanded graphite/polyaniline/$CoFe_2O_4$ ferrite, J. Mater. Chem. 22 (2012) 6449–6455.

[46] H. Zhu, H. Lin, H. Guo, L. Yu, Microwave absorbing property of Fe-filled carbon nanotubes synthesized by a practical route, Mater. Sci. Eng., B 138 (2007) 101–104.

[47] K.Y. Park, S.E. Lee, C.G. Kim, J.H. Han, Fabrication and electromagnetic characteristics of electromagnetic wave absorbing sandwich structures, Compos. Sci. Technol. 66 (2006) 576–584.

[48] P. Singh, V.K. Babbar, A. Razdan, R.K. Puri, T.C. Goel, Complex permittivity, permeability, and X-band microwave absorption of CaCoTi ferrite composites, J. Appl. Phys. 87 (2000) 4362–4366.

[49] P. Xu, X. Han, J. Jiang, X. Wang, X. Li, A. Wen, Synthesis and characterization of novel coralloid polyaniline/$BaFe_{12}O_{19}$ nanocomposites, J. Phys. Chem. C 111 (2007) 12603–12608.

[50] H. Lv, Y. Guo, Z. Yang, Y. Cheng, L.P. Wang, B. Zhang, Y. Zhao, Z.J. Xu, G. Ji, A brief introduction to the fabrication and synthesis of graphene based composites for the realization of electromagnetic absorbing materials, J. Mater. Chem. C 5 (2017) 491–512.

[51] S.S. Seyyed Afghahi, R. Peymanfar, S. Javanshir, Y. Atassi, M. Jafarian, Synthesis, characterization and microwave characteristics of ternary nanocomposite of MWCNTs/doped Sr-hexaferrite/PANI, J. Magn. Magn. Mater. 423 (2017) 152–157.

[52] S. Tyagi, H.B. Baskey, R.C. Agarwala, V. Agarwala, T.C. Shami, Development of hard/soft ferrite nanocomposite for enhanced microwave absorption, Ceram. Int. 37 (2011) 2631–2641.

[53] J.J. Jiang, D. Li, S.J. Li, Z.H. Wang, Y. Wang, J. He, W. Liu, Z.D. Zhang, Electromagnetic wave absorption and dielectric-modulation of metallic perovskite lanthanum nickel oxide, RSC Adv. 5 (2015) 14584–14591.

[54] W. Jing, Z. Hong, B. Shuxin, C. Ke, Z. Changrui, Microwave absorbing properties of rare-earth elements substituted W-type barium ferrite, J. Magn. Magn. Mater. 312 (2007) 310–313.

[55] E. Michielssen, J.M. Sajer, S. Ranjithan, R. Mittra, Design of lightweight, broad-band microwave absorbers using genetic algorithms, IEEE Trans. Microw. Theory Tech. 41 (1993) 1024–1031.